Engineering low-valent molybdenum sites in CoMoO$_4$ nanosheets to boost electrochemical nitrogen-rich wastewater treatment

Yuan Li [a,1], Xing Chen [b,1], Yu Yu [a,*], Kaifu Zhang [a], Yu Cheng [a], Weitao He [a], Qiquan Luo [b], Shan Gao [a,*]

[a] School of Chemistry and Chemical Engineering, Anhui Province Key Laboratory of Chemistry for Inorganic/Organic Hybrid Functionalized Materials, Anhui University, Hefei, Anhui 230601, China
[b] Institutes of Physical Science and Information Technology, Anhui University, Hefei 230601, China

ARTICLE INFO

ABSTRACT

Electrochemical coupling nitrate-to-ammonia (NO$_3^-$-to-NH$_3$) with urea oxidation reaction (UOR) is attractive for both energy-saving ammonia synthesis and comprehensive nitrogen-rich wastewater treatment. However, developing the efficient electrocatalyst that simultaneously promotes hydrogenation of NO$_3^-$ and UOR is still challenging. Here, we engineered the porous CoMoO$_4$ nanosheets with rich low-valent Mo sites (Mo$_{(L)}$-CoMoO$_{4-x}$) as a difunctional electrocatalyst for both NO$_3^-$-to-NH$_3$ and UOR. The Mo$_{(L)}$-CoMoO$_{4-x}$ displayed high Faradaic efficiency (93.33%) and selectivity (91.16%) for NO$_3^-$-to-NH$_3$ and low potential (1.31 V vs. RHE) at 100 mA cm^{-2} toward UOR. Impressively, a low cell voltage of 1.83 V was needed for coupling UOR with NO$_3^-$-to-NH$_3$ in two-electrode system. Mechanism study revealed that the introduction of low-valent Mo sites in CoMoO$_4$ nanosheets accelerated the activation kinetics and multistep hydrogenation of NO$_3^-$, and also promoted the reconstruction of active CoOOH species for UOR, resulting the difunctional catalytic property for NO$_3^-$-to-NH$_3$ and UOR.

1. Introduction

Nitrogen cycle is essential for the biosphere, but the global ever-increasing 'active' nitrogen through human activities has led to a serious imbalance in it and then triggered serious water pollution problems [1]. Typically, excess nitrate (NO$_3^-$) in surface and groundwater, caused by the overuse of N-containing fertilizers, industrial wastewater discharges and animal manures, has threatened the ecosystem and human health [2,3]. Electrocatalytic technology is an efficient and sustainable way for molecule conversion and energy storage [4–6], but the traditional electrochemical NO$_3^-$ removal is 'NO$_3^-$ to N$_2$', which can't achieve waste reuse. Proverbially, ammonia (NH$_3$) is one of the reduction products of NO$_3^-$ and possesses high economic value [7]. So, electrochemical converting NO$_3^-$ contaminant into NH$_3$ is attractive, which can simultaneously achieve nitrate removal and realize 'turn waste into wealth' [8–10]. However, the complex 8 e$^-$ coupled 9 H$^+$ transfer process urges the rational design of efficient electrocatalysts at the molecular level [11]. Additionally, in view of the high thermodynamic equilibrium potential (1.23 V vs. RHE) and sluggish

reaction kinetics of anodic oxygen evolution reaction (OER) during electrochemical NO$_3^-$ reduction reaction (NO$_3^-$RR) [12], alternative anodic reaction to OER is desirable to improve the energy efficiency. Urea is another contamination in the wastewater and the thermodynamic equilibrium potential of urea oxidation reaction (UOR, 0.37 V vs. RHE) is much lower than that of OER [13]. Thus, coupling the electrochemical UOR with NO$_3^-$RR is attractive which can efficiently improve the energy efficiency of both NO$_3^-$ and urea-rich wastewater treatment, simultaneously, realize waste recycle for ammonia synthesis. As well, efficient electrocatalysts for UOR is required. To reduce fabrication cost of catalytic material for coupled UOR and NO$_3^-$RR, a difunctional electrocatalyst that can be efficient for both NO$_3^-$-to-NH$_3$ and UOR is urgently desirable but the development of it is also an arduous task.

Cobalt (Co)-based materials have attracted much attention for electrochemical NO$_3^-$RR to NH$_3$ benefiting from their fascinating electronic structures [14,15]. Impressively, the oxidation-state Co compounds are favorable to the adsorption and activation of NO$_3^-$ due to the strong electrostatic interaction with NO$_3^-$ [3]. However, for the proton-coupled electron transfer reactions, sufficient active hydrogen supply from water

---

decomposition in non-acidic environment is also crucial for hydrogenation of the intermediates [16,17]. Unfortunately, the oxidation-state Co compounds usually show poor H_2O dissociation ability for sufficient active hydrogen generation [18]. Inspired by the high activity of low-valent molybdenum (Mo)-based materials at the edge for water dissociation [19,20], engineering oxidation-state Co compounds with low-valent Mo sites is expected for the synergetic NO_3^- activation and sufficient active hydrogen generation. On the other hand, as a difunctional electrocatalyst for NO_3^--to-NH_3 and UOR, the excellent UOR activity of Co-based material is of equal importance to reduce the energy efficiency. Commonly, the real active species of anodic Co-based materials for oxidation reaction, including the UOR, are the reconstructed high-valent Co compounds [21]. So, more available high-valent Co species could be reconstructed at the oxidative potential for the designed Co-based catalysts is crucial for excellent UOR activity.

Herein, we engineered the porous $CoMoO_4$ nanosheets with rich low-valent Mo sites grown on Ni foam (denoted as $Mo_{(L)}$-$CoMoO_{4-x}$) as an efficient difunctional electrocatalyst for both UOR and NO_3^--to-NH_3. The rich porous structure and oxygen vacancies of $CoMoO_4$ nanosheets induced the generation of low-valent Mo sites. The introduction of low-valent Mo sites in $CoMoO_4$ nanosheets not only accelerated the kinetics of NO_3RR, including the enhanced NO_3^- adsorption and the reaction rate, but also promoted the active hydrogen generation and the further hydrogenation of NO_3^- to NH_3. Expectedly, the $Mo_{(L)}$-$CoMoO_{4-x}$ showed superior performance toward NO_3RR with a high Faradaic efficiency (93.33%) and selectivity (91.16%) at –1.1 V vs. Ag/AgCl in 0.1 M Na_2SO_4 with 200 ppm NO_3^--N, much better than those of $CoMoO_4$. Impressively, when the Co-based nanosheets were used for UOR, in situ restructured CoOOH was verified to be the catalytic sites, and more CoOOH restructured in $Mo_{(L)}$-$CoMoO_{4-x}$ render it exhibited a low potential (1.31 V vs. RHE) at 100 mA cm^{-2} toward UOR, surpassing the $CoMoO_4$ and most reported electrocatalysts. Importantly, the bifunctional $Mo_{(L)}$-$CoMoO_{4-x}$ electrodes can be assembled into a two-electrode electrolyzer for coupling the UOR with NO_3RR, a low cell voltage of 1.83 V was needed to reach the current density of 100 mA cm^{-2}, and the selectivity of NH_3 can remain over 90% after five cycles.

2. Experimental section

2.1. Material synthesis

2.1.1. Synthesis of $Mo_{(L)}$-$CoMoO_{4-x}$ nanosheets supported on Ni foam

Before the preparation, Ni foam substrate was sonicated with acetone, 0.3 M HCl aqueous solution, and deionized water for 30 min, respectively, to remove the surface oxide layer and organic molecules. Typically, 0.484 g Na_2MoO_4 and 0.582 g $Co(NO_3)_2 \cdot 6 H_2O$ were dissolved into 30 mL deionized water under lightly stirring to form a transparent solution. Then, the solution was transferred to the 50 mL of Teflon-lined autoclave, along with the vertical placement of one piece of pre-treated Ni foam, and heated at 160 °C for 6 h. After cooling to room temperature, the CoMo-precursors were collected by washing with water and ethanol several times and then dried in a vacuum drier for 12 h. The final product was calcined at 400 °C for 2 h with heating rate of 2 °C min^{-1} under $H_2/Ar(v/v = 10\%/90\%)$ mixed reductive atmosphere, and then naturally cooled to ambient temperature.

2.1.2. Synthesis of $CoMoO_4$ nanosheets supported on Ni foam

The above CoMo-precursors were calcined at 400 °C for 2 h with heating rate of 2 °C min^{-1} under an oxidative atmosphere, and then naturally cooled to ambient temperature.

2.1.3. Synthesis of $CoMoO_{4-x}$ nanosheets supported on Ni foam

The as-prepared $CoMoO_4$ nanosheets were calcined at 400 °C for 0.5 h with heating rate of 5 °C min^{-1} under H_2/Ar (v/v = 5%/95%) mixed gas atmosphere, and then naturally cooled to ambient temperature.

2.2. Catalyst characterization

X-ray diffraction (XRD) patterns were collected using Cu Kα radiation on a Smart Lab 9 kW powder X-ray diffractometer. Before the XRD test, the as-prepared nanosheets was sonicated and collected from the Ni foam. The morphology was characterized by using field-emission scanning electron microscopy (SEM, Hitachi S-4800, 20 kV). Transmission electron microscopy (TEM) and high-resolution TEM images were obtained on a JEM-2100 transmission electron microscope (EOL). X-ray photoelectron spectroscopy (XPS) was measured by an ESCALAB 250Xi spectrometer equipped with an aluminum anode (Al Kα = 1846.6 eV). The binding energy was determined using the C 1 s spectrum at 284.8 eV as a reference. The specific surface area was obtained by the Brunauer-Emmett-Teller (BET) method and measured by using a Micromeritics ASAP 2020 at 77 K with N_2 physical adsorption. ^1H NMR experiments were performed using Bruker 600 MHz, D_2O as deuterium reagent. In situ characterization of the working electrode was performed using a Nicolet iS50 FTIR spectrometer (Thermo Scientific, Warsaw, Poland). Raman spectra were recorded on an Olympus BX40 system with a 50x long working-length objective (HORIBA Scientific, France) instrument with an Nd: YAG laser source of 638 nm.

2.3. Electrochemical measurements

2.3.1. Electrochemical measurements of nitrate reduction reaction

All electrochemical measurements were conducted on a CHI 760E electrochemical workstation. The catalysts grown on Ni foam (1.0 cm × 1.0 cm), Ag/AgCl electrode, and Pt foil were used as working electrode, reference electrode, and counter electrode, respectively. In a typical H-cell system, 0.1 M Na_2SO_4 solution was evenly dispersed into the cathode and anode chambers, and an additional 200 ppm NO_3^--N was added to the cathode chamber. It was necessary to feed the cathode electrolyte with Ar for 30 min to remove the dissolved oxygen before conducting the electrochemical tests. LSV curves were performed with a scan rate of 10 mV s^{-1} from –0.6 to –1.6 V vs. Ag/AgCl. Then, the chronoamperometry tests were carried out at different potentials for 2 h. The electrochemical active surface area (ECSA) of the sample was calculated from the double layer capacitance (C_{dl}) according to the following equation: ECSA = C_{dl} / C_s, where C_s is the specific capacitance of the sample. To measure the C_{dl}, cyclic voltammetry (CV) tests were performed at different sweep rates from 10 to 50 mV s^{-1}. Consider that the specific capacitance for a flat surface is generally in the range of 20–60 μF cm^{-2}. We used the value of 40 μF cm^{-2} for ECSA calculations.

2.3.2. Electrochemical measurements of urea oxidation reaction

The catalysts grown on Ni foam (1.0 cm×1.0 cm), Hg/HgO electrode, and Pt foil were used as working electrode, reference electrode, and counter electrode, respectively. The electrolyte solution consists of 1.0 M KOH and 0.33 M urea. LSV tests were performed from 0.7 to 1.8 V vs. RHE at a scan rate of 10 mV s^{-1} and with 50% *iR* compensation. All potentials measured are calibrated to a reversible hydrogen electrode (RHE) as Equation Eq. (1):

$$E_{RHE} = E_{Hg/HgO} + 0.0591 \times pH + 0.098 \tag{1}$$

2.3.3. Electrochemical coupling NO_3^--to-NH_3 and UOR measurements

For two-electrode electrolysis, $Mo_{(L)}$-$CoMoO_{4-x}$ electrode is employed as both anode and cathode. 1.0 M KOH with 0.33 M urea was used as anodic electrolyte for UOR and 1.0 M KOH with 200 ppm NO_3^--N was used as cathodic electrolyte for nitrate reduction. All experiments are carried out at room temperature.

2.3.4. In situ electrochemical measurements

In situ FTIR tests were performed using a Nicolet iS50 FTIR spectrometer. Typically, 5 mg of catalysts and 20 μL of Nafion solution were dispersed in 0.3 mL ethanol and 0.2 mL water solution by sonication for

0.5 h. Then the mixed solution was loaded onto the Au-coated Si crystal and dried naturally for further use. All electrochemical tests were measured in 0.1 M Na_2SO_4 electrolyte with 200 ppm NO_3^--N and controlled by a CHI 760E electrochemical workstation.

In situ Raman measurement was carried out by the Raman microscope and electrochemical workstation. The cell was designed by Teflon with a quartz window between the sample and the objective. All electrochemical tests were measured in 0.1 M Na_2SO_4 electrolyte with 200 ppm NO_3^--N and controlled by a CHI 760E electrochemical workstation.

2.4. Determination of ion concentration

2.4.1. Determination of NO_3^--N concentration

Nitrate concentrations were measured following standard methods [22]. 0.1 mL 1 M HCl and 0.01 mL sulfamic acid solution (0.8 wt%) were added into the solution and waited for 20 min to texting. Using a UV-Vis spectrophotometer measured the absorption spectra and recorded the absorption intensities at 220 nm and 275 nm. The final absorbance value was calculated by this equation: A = A_{220nm} − $2A_{275nm}$.

2.4.2. Determination of NO_2^--N concentration

Nitrite concentrations were analyzed using the Griess test with slight modification [23]. The color reagent was prepared by dissolving 0.2 g of N-(1-naphthyl) ethylenediamine dihydrochloride, 4.0 g of sulfonamide, and 10 mL H_3PO_4 in appropriate deionized water. Then the mixed solution was volumed to be 100 mL with the distilled water. 0.1 mL color reagent was added into the solution and mixed uniformity, and the absorption intensity at a wavelength of 540 nm was recorded after standing for 20 min.

2.4.3. Determination of NH_4^+-N concentration

The quantity of NH_3 product was determined via a colorimetric method using Nessler's reagent [23]. The Nessler's reagent was prepared by dissolving 7 g KI and 10 g HgI_2 in 100 mL 4.0 M NaOH solution successively and then the mixed solution was placed in the dark without disturbance for 24 h. Finally, the supernatant liquid was transferred into a Teflon bottle refrigerated for use. For the colorimetric assay, 0.1 mL potassium sodium tartrate solution (ρ = 500 g L^{-1}) was added and mixed thoroughly, and then 0.1 mL Nessler's reagent was put into the solution. The absorption intensity at a wavelength of 420 nm was recorded after standing for 20 min.

2.5. Calculation of the conversion, selectivity, Faradaic efficiency, and yield

The selectivity of NH_3 was calculated according to Eq. (2)

$$Selectivity\ (S_{NH_3})\ =\ C_{NH_3}\ /\ \Delta C_{NO_3^-}\ \times\ 100\% \tag{2}$$

The Faradaic efficiency of electroreduction of NO_3^- to NH_3 was calculated according to Eq. (3):

$$Faradaic\ efficiency\ (FE)\ =\ (8\ F\ \times\ C_{NH_3}\ \times\ V)\ /\ (14\ \times\ Q) \tag{3}$$

The yield rate of NH_3 was calculated according to Eq. (4):

$$Yield\ rate\ of\ NH_3\ (\mu mol\ h^{-1}\ cm^{-2})\ =\ (C_{NH_3}\ \times\ V)\ /\ (14\ \times\ t\ \times\ s) \tag{4}$$

$\Delta C_{NO_3^-}$ is the concentration difference of NO_3^--N (ppm) before and after electrolysis, C_{NH_3} is the concentration of NH_4^+-N (ppm), F is the Faradaic constant (96485 C mol^{-1}), Q is the total charge passing the electrode (C), V is the volume of electrolyte in the cathode compartment

(35 mL), t is the electrolysis time (2 h), s is the geometric area of working electrode (1 cm^{-2}).

2.6. Calculational methods

All density functional theory (DFT) calculations were conducted using the Vienna ab initio simulation package (VASP), based on first principles [24,25]. The study utilized the projector augmented wave (PAW) method and the Perdew-Burke-Ernzerhof (PBE) exchange-correlation functional, incorporating spin polarization [26–28]. A 15 Å vacuum space was introduced to prevent interactions between adjacent layers. Calculations used a cutoff energy of 450 eV, achieving convergence with tolerances of 10^{-5} eV for energy and 0.01 eV $Å^{-1}$ for forces. A gamma-centered (3×3×4) k-point grid was used for Brillouin zone sampling in the bulk. TEM and XRD results determined the lattice parameters of ferromagnetic bulk $CoMoO_4$ as a = 10.165 Å, b = 9.238 Å, c = 7.003 Å, $\alpha = \gamma = 90.000°$, and $\beta = 106.963°$, indicating a monoclinic *C12/m1* symmetry [29]. In this structure, each Co atom is surrounded by six oxygen atoms, and each Mo atom by four, forming hexahedral and tetrahedral units, respectively. The (001) surface was chosen as the model surface. Hubbard parameters (U) of 4.38 for Mo and 3.32 for Co were consistently applied to address onsite electron correlation in d orbitals across all calculations [29]. The CI-NEB method was employed to identify transition states [30].

The calculation of Gibbs free energy change (ΔG) relies on the computational hydrogen electrode (CHE) model proposed by Nørskov and colleagues [31,32]:

$$\Delta G\ =\ \Delta E\ +\ \Delta E_{ZPE} - T\Delta S \tag{5}$$

ΔE, ΔE_{ZPE}, and ΔS refer to the differences in energy, zero-point energy, and vibrational entropy, respectively, between the final and initial surface species for each elementary step of adsorption, desorption, and protonation.

The adsorption energies of NO_3^- (ΔG_{*NO3}) on $CoMoO_4$ and $Mo_{(L)}$-$CoMoO_{4-x}$ are determined using the expression below:

$$\Delta G_{*NO3}\ =\ G_{NO_3^-} - G_* -\ G_{HNO3}\ +\ 0.5G_{H2(g)} - \Delta G_{correct} \tag{6}$$

Where ΔG_{*NO3} and G_* indicate the energies of $CoMoO_4$ and $Mo_{(L)}$-$CoMoO_{4-x}$ with NO_3^- adsorbed, respectively. Meanwhile, $G_{HNO3}(g)$ and $G_{H2}(g)$ denote the energies of gaseous HNO_3 and H_2 molecules, with a correction factor $\Delta G_{correct}$ of 0.392 eV [33].

3. Results and discussion

3.1. Catalyst preparation and characterization

The porous $CoMoO_4$ nanosheets with rich low-valent Mo sites grown on Ni foam ($Mo_{(L)}$-$CoMoO_{4-x}$) were successfully fabricated through rapid calcination of the CoMo-precursors in the reductive atmosphere (See details in Experimental section). The schematic of structures of $Mo_{(L)}$-$CoMoO_{4-x}$ was depicted in Fig. 1a. Scanning electron microscopy (SEM) images of $Mo_{(L)}$-$CoMoO_{4-x}$ shows interconnected and ordered nanosheets array structure grown on the substrate with the average thickness of the nanosheets is ~37 nm (Fig. 1b, S1). Then, we can see abundant pores in the two-dimensional $Mo_{(L)}$-$CoMoO_{4-x}$ nanosheets from the transmission electron microscopy (TEM) images (Fig. 1c, S2). And a typical interplanar lattice fringe of 0.231 nm is observed in the high-resolution TEM (HRTEM) image (inset of Fig. 1c), which corresponds to the $CoMoO_4$ (040) plane. Impressively, the lattice fringe at the edge of the pore is ambiguous, which may be attributed to the formation of low-valent Mo sites induced by the oxygen vacancies (O_{vac}). The scanning TEM energy dispersive X-ray spectroscopy (EDS) mapping images (Fig. S3) indicate the existence and uniform distribution of Co, Mo and O in $Mo_{(L)}$-$CoMoO_{4-x}$. For comparison, $CoMoO_4$ nanosheets were also fabricated through the calcination of the CoMo-precursors in oxidative
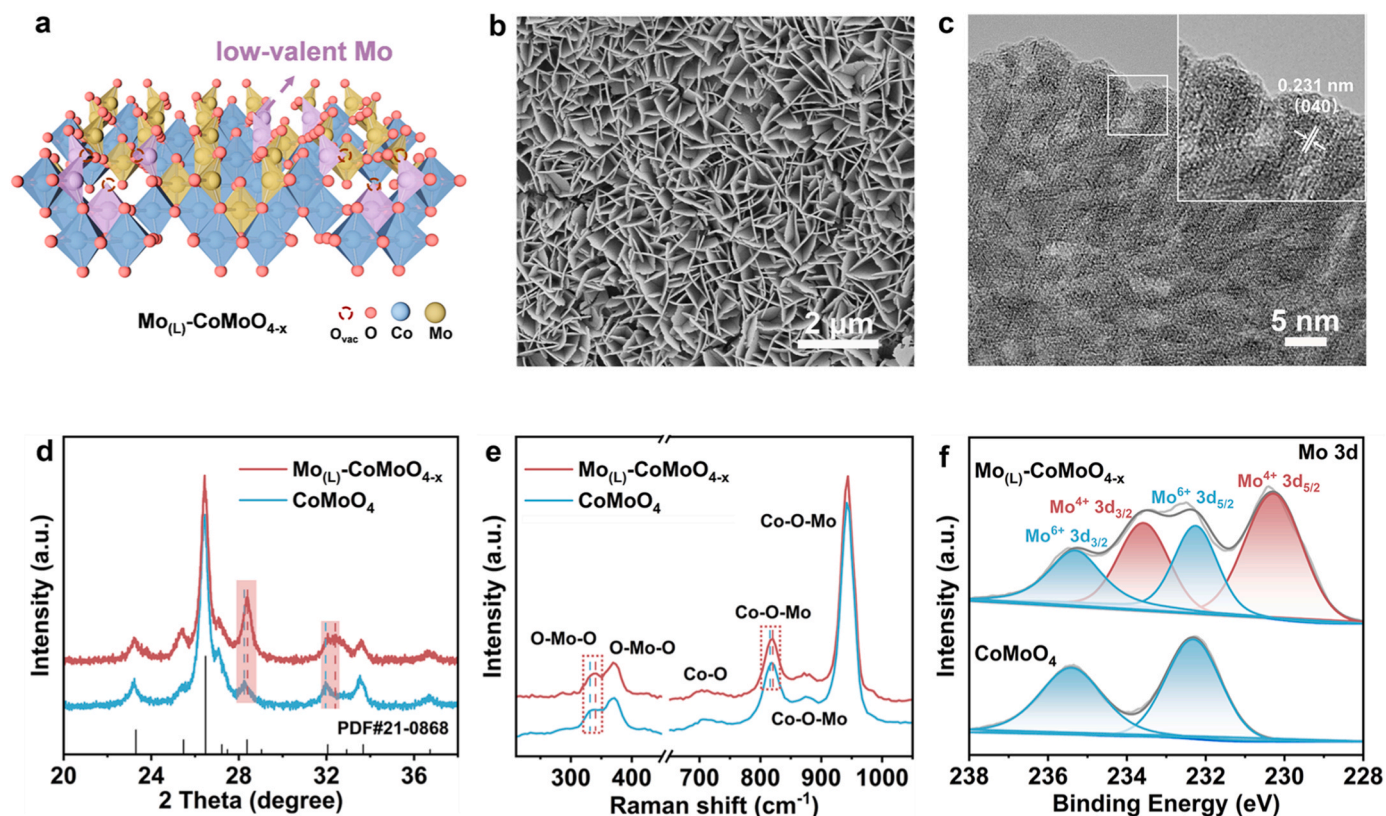
Fig. 1. (a) Crystal structure of the $Mo_{(L)}$-$CoMoO_{4-x}$. (b) SEM and (c) HRTEM image of $Mo_{(L)}$-$CoMoO_{4-x}$. (d) XRD patterns, (e) Raman spectra and (f) Mo 3d XPS spectra of $Mo_{(L)}$-$CoMoO_{4-x}$ and $CoMoO_4$.

atmosphere. The analogous morphology of the $CoMoO_4$ nanosheets can be seen from Fig. S4, S5a. But a small number of pores and orderly lattice fringes could be seen in $CoMoO_4$ nanosheets (Fig. S5b). The Brunauer-Emmett-Teller (BET) surface area analysis result indicates that the BET surface area of $Mo_{(L)}$-$CoMoO_{4-x}$ is

39.5 m^2 g^{-1}, much larger than that of $CoMoO_4$ (11.63 m^2 g^{-1}), further confirming the porous structure of $Mo_{(L)}$-$CoMoO_{4-x}$ (Fig. S6). X-ray diffraction (XRD) patterns (Fig. 1d) identify the as-prepared nanosheets as monoclinic $CoMoO_4$ (JCPDS No. 21–0868). Moreover, partial diffraction peaks (marked with pink background) show slight shifts to high angles and broadening in $Mo_{(L)}$-$CoMoO_{4-x}$ compared to those of $CoMoO_4$, indicating the existence of O_{vac} and porous structure, respectively [34]. In the Raman spectra (Fig. 1e), the peaks located at 337 and 370 cm^{-1} are ascribed to asymmetric and symmetric bending modes of the O-Mo-O, respectively, and the symmetric stretching of the Co-O bond locates at 706 cm^{-1}. Moreover, the modes located at 819, 875 and 943 cm^{-1} could be indexed to asymmetric stretching modes of oxygen in binding Co-O-Mo [35]. Notably, the peaks located at 337 and 819 cm^{-1} in $Mo_{(L)}$-$CoMoO_{4-x}$ shifte slightly toward higher wavenumber, confirming the existence of O_{vac} in $Mo_{(L)}$-$CoMoO_{4-x}$ [36,37]. This is also revealed by O 1 s X-ray photoelectron spectra (XPS) (Fig. S7), in which the binding energy of 531.4 eV could be ascribed to O_{vac} and the proportion of O_{vac} in $Mo_{(L)}$-$CoMoO_{4-x}$ is much higher than that in $CoMoO_4$ [38]. On account of the abundant pore and O_{vac}, low-valent Mo (Mo^{4+}) is induced in $Mo_{(L)}$-$CoMoO_{4-x}$, which is revealed by the high-resolution XPS of Mo 3d. As shown in Fig. 1f, except for the normal high-valent Mo^{6+} located at 232.2 and 235.3 with a bandgap of 3.1 eV, low-valent Mo (230.3 and 233.6 eV) was also detected in $Mo_{(L)}$-$CoMoO_{4-x}$, which did not exist in $CoMoO_4$ [35]. The binding energies of 796.90, 780.90, 803.0, 786.5 eV in $CoMoO_4$ were in good agreement with Co^{2+} $2p_{1/2}$, $2p_{3/2}$, and their satellite peaks, respectively (Fig. S8) [39]. And a slight positive shift of binding energy for Co 2p in $Mo_{(L)}$-$CoMoO_{4-x}$ indicates slight reduction of Co^{2+}. Based on the above analysis, low-valent Mo

(Mo^{4+}) was induced in $Mo_{(L)}$-$CoMoO_{4-x}$ nanosheets benefited from the abundant pores and oxygen vacancies.

3.2. Electrocatalytic performance for NO_3^--to-NH_3

Profited from the low-valent Mo induced by the porous structure and oxygen vacancies, $Mo_{(L)}$-$CoMoO_{4-x}$ nanosheets exhibit outstanding electrochemical NO_3^--to-NH_3 performance. The electrochemical tests were performed in conventional H-cell with different electrolyte compositions under ambient conditions. Firstly, the linear sweep voltammetry (LSV) curves of different electrodes in 0.1 M Na_2SO_4 with and without 200 ppm NO_3^--N were shown in Fig. 2a. All of the samples exhibit higher current densities in 0.1 M Na_2SO_4 with NO_3^- addition than those measured in 0.1 M Na_2SO_4 and $Mo_{(L)}$-$CoMoO_{4-x}$ shows the maximum current density, indicating the highest activity of $Mo_{(L)}$-$CoMoO_{4-x}$ for the NO_3^-RR. To insight the intrinsic catalytic activity of different catalysts, the electrochemical active surface area (ECSA) of the samples were tested (Fig. S9). The the ECSA-normalized LSV curves with 200 ppm NO_3^--N were plotted (Fig. S10), and the $Mo_{(L)}$-$CoMoO_{4-x}$ still shows larger normalized current density than that of $CoMoO_4$, indicating the better intrinsic activity of $Mo_{(L)}$-$CoMoO_{4-x}$. Then, chronoamperometry tests at different potentials were applied to accumulate the reduction products of NO_3^-, and the concentrations of residual NO_3^- and the products were analyzed using the colorimetric methods (See the standard curves in Fig. S11, S12). The production of NH_3 in the electrolytes with and without 200 ppm NO_3^--N were first quantified, and very little NH_3 can be detected in the electrolytes without NO_3^-, indicating that the production of NH_3

originated from the electroreduction of nitrate (Fig. S13). To ensure the accuracy of colorimetric methods for NH_3 quantification, ^1H nuclear magnetic resonance (NMR) spectra were also carried out using maleic acid as internal standard, and the standard curve was depicted based on the signals of standard solutions with gradient concentrations (inset of
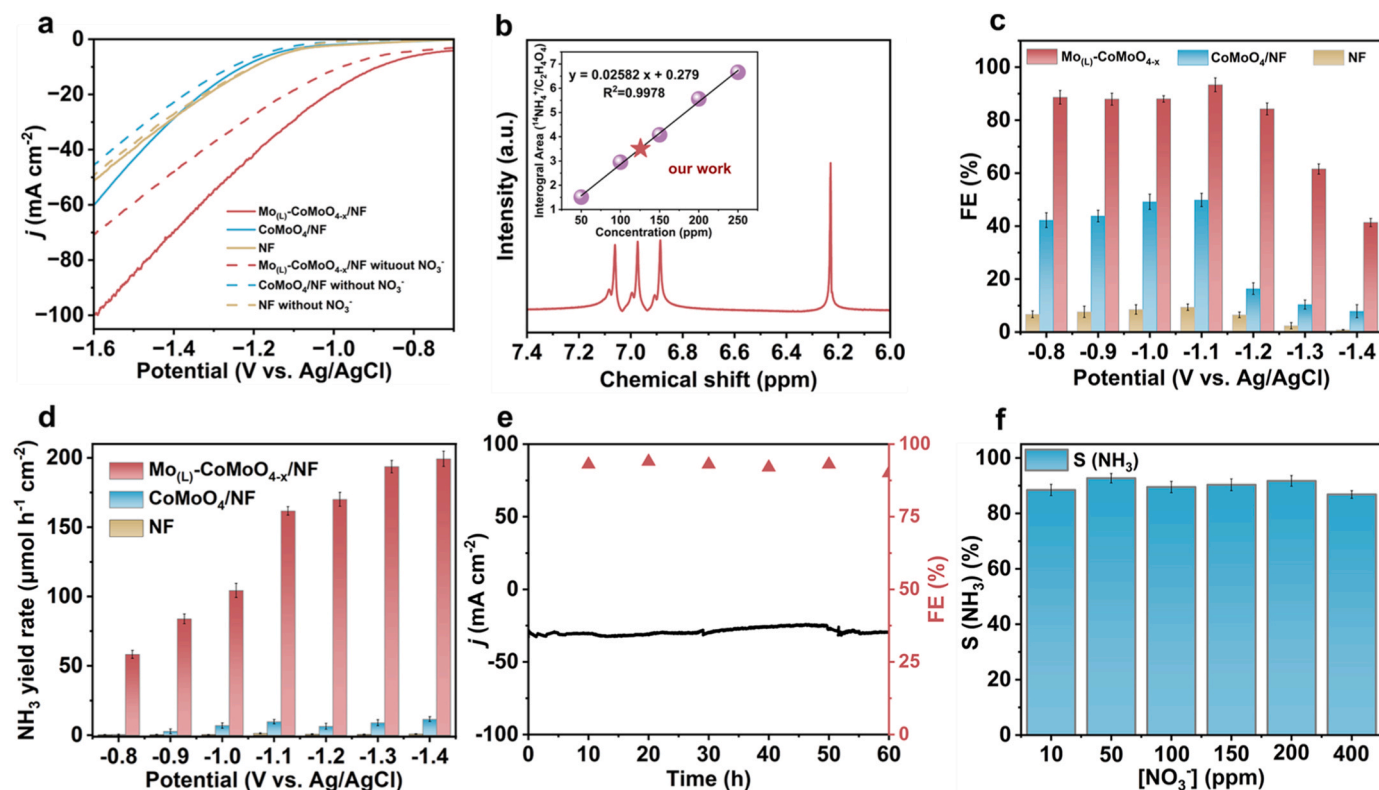
Fig. 2. (a) LSV curves of the prepared samples with and without 200 ppm NO_3^--N. (b) The ^1H NMR signal after electrocatalytic NO_3^-RR, insert is the standard curve. (c) FEs of NH_3 and (d) NH_3 yield rates of the prepared samples at different potentials. (e) Chronoamperometry test of $Mo_{(L)}$-$CoMoO_{4-x}$ in the flowing 0.1 M Na_2SO_4 with 200 ppm NO_3^--N electrolyte. (f) The selectivity of NH_3 in the electrolyte with different initial NO_3^- concentrations for $Mo_{(L)}$-$CoMoO_{4-x}$.

Fig. 2b, S14). The ^1H NMR signal of the post-test electrolyte with 200 ppm NO_3^--N were shown in the inset of Fig. 2b and NH_4^+ yield was quantified to be 156.7 μmol h^{-1} cm^{-2}. In addition, to clarify the source of ammonia and more accurately quantify the produced NH_4^+, we used $K^{15}NO_3$ as the feeding N-source to perform the isotopic labeling NO_3^- experiments. ^1H NMR spectra were carried out and the standard curve was depicted based on the signals of standard $(^{15}NH_4)_2SO_4$ solutions with gradient concentrations (Fig. S15a and inset of Fig. S15b). The ^1H NMR signal of the post-test electrolyte with 200 ppm $^{15}NO_3^-$-N was shown in Fig. S15b, and the $^{15}NH_4^+$ yield was quantified to be 157.5 μmol h^{-1} cm^{-2}, which is close to the quantitative results of $^{14}NH_4^+$ ^1H NMR and colorimetric methods (Fig. S16)[40]. Based on the accurate detection, the Faraday efficiencies (FEs) of NH_3(aq) as well as the NH_3 yield at different potentials over different samples from –0.8 to –1.4 V vs. Ag/AgCl were calculated and showed in Fig. 2c, d. Obviously, $Mo_{(L)}$--$CoMoO_{4-x}$ always showed the maximum FE and NH_3 yield under the same potential and the highest FE of NH_3 over $Mo_{(L)}$-$CoMoO_{4-x}$ could reach 93.33% at the low potential of –1.1 V vs. Ag/AgCl. This performance is superior to most reported electrocatalysts in the neutral electrolytes (Table S1). Meanwhile, the $Mo_{(L)}$-$CoMoO_{4-x}$ also exhibited the highest NH_3 partial current densities ($j_{Ammonia}$), indicating its highest activity for NO_3^--to-NH_3 (Fig. S17). Furthermore, very few NO_2^- were detected at all potentials (Fig. S18), further demonstrating the high selectivity of $Mo_{(L)}$-$CoMoO_{4-x}$. To evaluate the long-term stability of $Mo_{(L)}$-$CoMoO_{4-x}$, we performed the chronoamperometry tests at –1.1 V vs. Ag/AgCl in the flowing 0.1 M Na_2SO_4 with 200 ppm NO_3^--N electrolyte to ensure stable NO_3^- supply. As shown in Fig. 2e, the current density can maintain for 60 h and no obvious decline of the FE of NH_3 can be seen, indicating the excellent stability of $Mo_{(L)}$-$CoMoO_{4-x}$. Moreover, successive recycling tests at –1.1 V vs. Ag/AgCl for $Mo_{(L)}$--$CoMoO_{4-x}$ demonstrate that FE and selectivity of NH_3 could maintain well after six cycles (Fig. S19). And the remained nanosheet morphology (Fig. S20) and electronic states of Mo and O (Fig. S21) after the cycling

test further confirm the good stability.

To further evaluate the capability of $Mo_{(L)}$-$CoMoO_{4-x}$ for NO_3^- treatment, the concentration of NO_3^--N in the electrolyte was degraded from 400 to 10 ppm, and the chronoamperometry tests were conducted at –1.1 V vs. Ag/AgCl for 2 h. As shown in Fig. 2f, the selectivity of NH_3 showed no obvious decay as the decrease of the NO_3^- concentration. Futhermore, the continuous 20 h chronoamperometry tests at –1.1 V vs. Ag/AgCl in the flowing 0.1 M Na_2SO_4 with 10, 200 and 400 ppm NO_3^--N electrolyte, respectively, were conducted (Fig. S22). No obvious decay of current density as well as the FE of NH_3 can be seen, suggesting the good application potential of $Mo_{(L)}$-$CoMoO_{4-x}$ for NO_3^- containing wastewater removal. These reults confirm that the engineering of low-valent Mo efficiently improve the electrochemical NO_3^--to-NH_3 performance of $CoMoO_4$. To further confirm the key role of the low-valent Mo, we also fabricated the $CoMoO_4$ nanosheets with oxygen vacancies but no low-valent Mo (labeled as $CoMoO_{4-x}$) (Fig. S23, S24) and measured their catalytic performance for NO_3^--to-NH_3. As shown in Fig. S25, $CoMoO_{4-x}$ shows the optimal FE (61.42%) of NH_3 at the potential of –1.1 V vs. Ag/AgCl and highest NH_3 yield of 24.11 μmol h^{-1} cm^{-2} at –1.4 V vs. Ag/AgCl, little better than those of $CoMoO_4$ (49.87%, 11.53 μmol h^{-1} cm^{-2}). Based on these results, we further confirm the key role of the low-valent Mo for improving catalytic performance $CoMoO_4$.

3.3. Mechanism study of the excellent performance for NO_3^--to-NH_3

To understand the origin of the remarkable and enhanced performance of $Mo_{(L)}$-$CoMoO_{4-x}$ electrocatalyst for NO_3^-RR, the kinetic study was performed. Firstly, we carried out the Raman spectra of $Mo_{(L)}$-$CoMoO_{4-x}$ and $CoMoO_4$ in the electrolytes with NO_3^- to explore the NO_3^-adsorption capacity on the surface. As shown in Fig. 3a, the characteristic peaks located at 1060 cm^{-1} corresponding to the symmetric NO_3^- stretching can be observed [41], and the intensity over on $Mo_{(L)}$--$CoMoO_{4-x}$ is obviously stronger than that over $CoMoO_4$, suggesting the
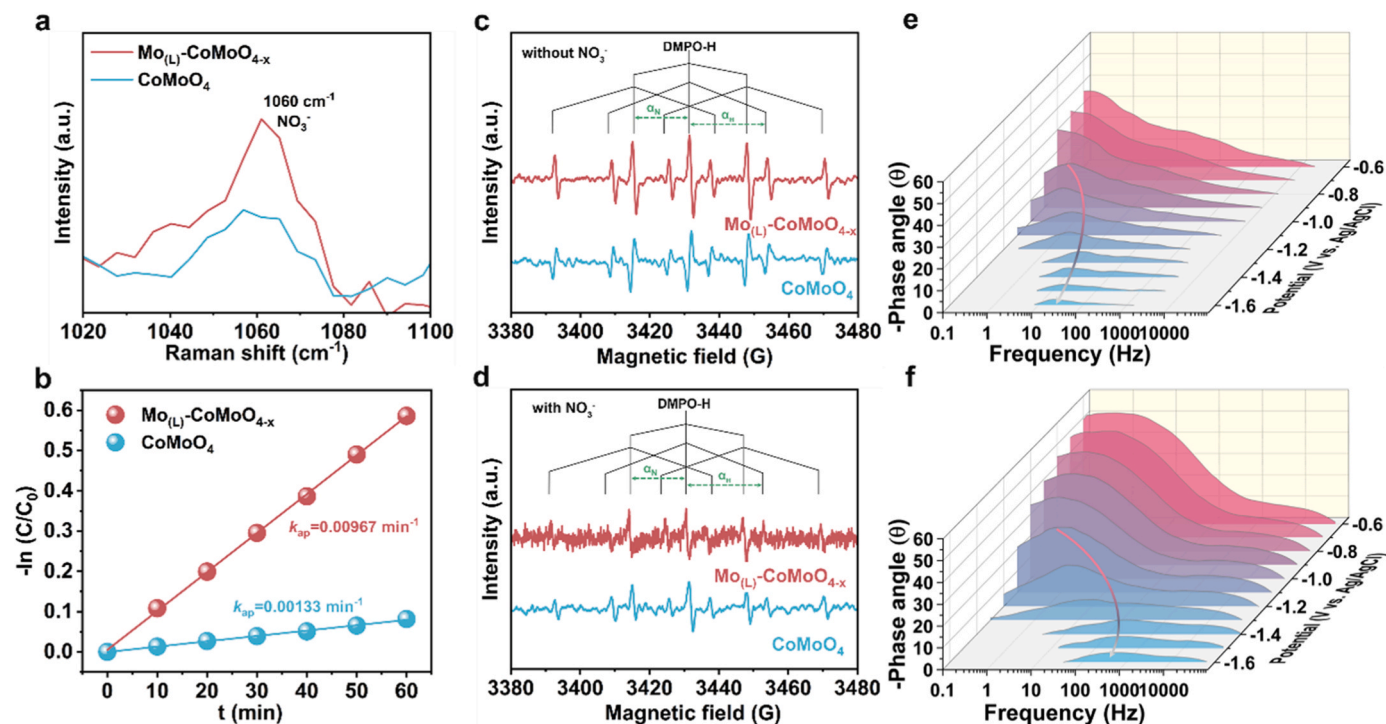
Fig. 3. (a) Raman spectra of the samples in the electrolyte with NO_3^-. (b) pseudo first-order reactions of NO_3^-RR. (c, d) DMPO spin-trapping EPR spectra of the electrolyte with and without NO_3^-. The Bode plots of (e) $Mo_{(L)}-CoMoO_{4-x}$ and (f) $CoMoO_4$.

better NO_3^- adsorption capacity of $Mo_{(L)}-CoMoO_{4-x}$ [42]. Then, during the electrolysis process, the time-dependent concentration variations of different ions over $Mo_{(L)}-CoMoO_{4-x}$ were recorded (Fig. S26) and the reaction kinetics could be deduced. As shown in Fig. 3b, pseudo first-order reactions of NO_3^-RR over $Mo_{(L)}-CoMoO_{4-x}$ and $CoMoO_4$ are observed [43]. And first reaction order could also be confirmed by the plots of the total current densities at –1.1 V vs. Ag/AgCl against the NO_3^- concentrations (ppm) (Fig. S27) [44]. The apparent reaction rate constant (k_{ap})

calculated through the slope of the linear fitting of $Mo_{(L)}-CoMoO_{4-x}$ is 7.2-fold higher than that of $CoMoO_4$, indicating the faster reaction rate of $Mo_{(L)}-CoMoO_{4-x}$ for NO_3^- ions activation, which is challenging for most of the reported electrocatalysts [45–47]. Beside the adsorption and activation of NO_3^-, the generation and consumption of active hydrogen (*H) is crucial for the hydrogenation of nitroxide intermediates to NH_3. To evaluate the ability of generated/consumed *H during the NO_3^-RR, we monitored the amounts of *H through operando electron paramagnetic resonance (EPR) using 5,5-dimethyl-1-pyrroline N-oxide (DMPO) as an *H trapping reagent [48]. During the electrolysis in the electrolyte without NO_3^-, the singles of *H with nine typical strong peaks (intensity ratio: 1:1:2:1:2:1:2:1:1) are observed (Fig. 3c), and the intensity of *H single over $Mo_{(L)}-CoMoO_{4-x}$ was much stronger than that of $CoMoO_4$, suggesting the better ability of $Mo_{(L)}-CoMoO_{4-x}$ to drive the H_2O dissociation to generate *H. After adding NO_3^- in the electrolyte (Fig. 3d), the signal intensity of DMPO-H decreased dramatically over $Mo_{(L)}-CoMoO_{4-x}$ but slightly over $CoMoO_4$, indicating the faster consumption of the *H on $Mo_{(L)}-CoMoO_{4-x}$ during NO_3^-RR process [17,18]. Additionally, the Bode plots (Fig. 3e, f) of $Mo_{(L)}-CoMoO_{4-x}$ and $CoMoO_4$ showed that the characteristic peak associated with the adsorption of *H centered at $\approx10^0$ Hz emerged at –0.9 V vs. Ag/AgCl over $Mo_{(L)}-CoMoO_{4-x}$, lower than that of $CoMoO_4$ (–1.1 V vs. Ag/AgCl), confirming the better *H generation ability of $Mo_{(L)}-CoMoO_{4-x}$ [49]. And during NO_3^-RR, the peak shifts to high frequencies with increasing applied potentials and a lower phase angle of $Mo_{(L)}-CoMoO_{4-x}$ confirmed the faster charge transfer and hydrogenation rate of NO_3^- reduction to NH_3 [50]. These kinetic study results proved that the construction of low-valent

Mo sites in $CoMoO_4$ nanosheets could promote the adsorption, activation and hydrogenation of NO_3^- to NH_3.

In addition, we conducted in situ Fourier transform infrared spectrum (FTIR) and Raman to monitor the intermediates during the reduction reaction. The in situ FTIR spectra of $Mo_{(L)}-CoMoO_{4-x}$ and $CoMoO_4$ at different potentials from –0.7 to –1.5 V vs. Ag/AgCl were tested. As shown in Fig. 4a, the positive peak located at 1337 cm^{-1} can be assigned to N-O asymmetric stretching vibration of NO_3^- and the weak intensity indicates the consumption of NO_3^- [41]. Then, the bands at 1296 and 1557 cm^{-1} can be assigned to the deoxidation intermediates of *NO_2 and *NO, respectively [51]. At the same time, the peaks located at 1100, 1435, 1506, 1539 cm^{-1} correspond to the protonation intermediates of *NH_2OH, *NH_2, *NH, *HNO, respectively [17,41,52,53], and the produced NH_4^+ (1456 cm^{-1}) 1 s also detected. The intensities of both deoxidation and protonation intermediates are gradually increased as the potential increased, suggesting $Mo_{(L)}-CoMoO_{4-x}$ could efficiently promote the activation and protonation of NO_3^- and the eventual generation of NH_3. In comparison, the same deoxidation and protonation intermediates could be detected on the $CoMoO_4$ during NO_3^-RR, but their intensities are much weaker than those of $Mo_{(L)}-CoMoO_{4-x}$. Particularly, hydroxylamine (*NH_2OH) is the key intermediate for NH_3 formation [41], the band intensity of *NH_2OH (located at 1100 cm^{-1}) on $CoMoO_4$ is distinctly weaker than that on $Mo_{(L)}-CoMoO_{4-x}$, thus resulting the poor performance for NO_3^- to NH_3. Then, in situ Raman spectra at different potentials were shown in Fig. S28. The vibration bands at 1060 cm^{-1} could be assigned to the symmetric stretching of NO_3^-, and the intermediates of NO_2 (1190 cm^{-1}), HNH (1312 cm^{-1}), NH_3 (1430 cm^{-1}) could also be detected during the NO_3^-RR electrolysis [41,54,55]. Based on the intermediates detected by in situ FTIR and Raman and many reported works [56–58]. we derived the possible NO_3^-RR reaction path on the surface of the electrocatalysts as shown in Fig. 4c. The NO_3^-RR process included two steps: deoxygenation reactions ($NO_3^- \rightarrow NO_2^- \rightarrow NO$) and hydrogenation steps ($NO \rightarrow HNO \rightarrow H_2NO \rightarrow NH_2OH \rightarrow$ *$NH_2 \rightarrow NH_3$). And the schematic diagram of NO_3^-RR on the surface of $Mo_{(L)}-CoMoO_{4-x}$ could be depicted in Fig. S29, in which the promoted generation of the key NH_2OH intermediate on $Mo_{(L)}-CoMoO_{4-x}$ showed great
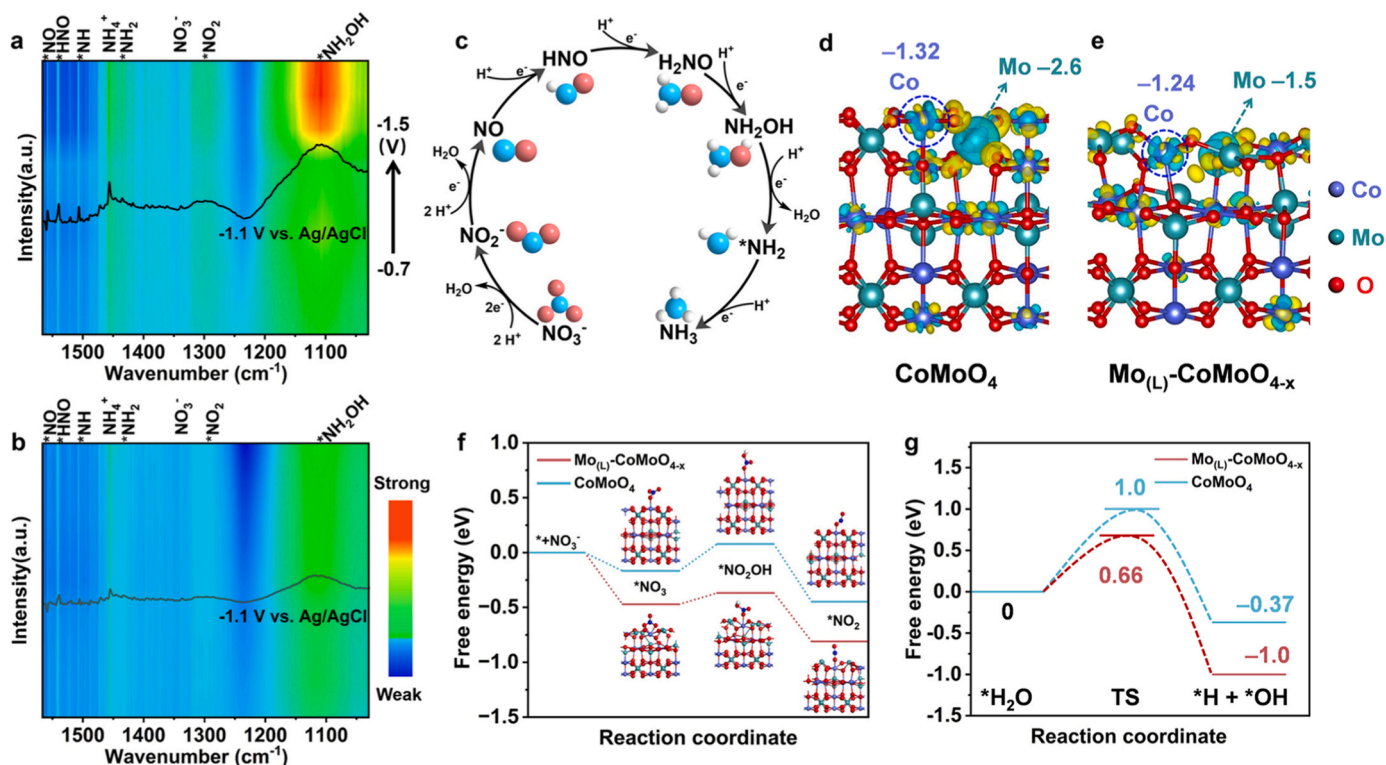
Fig. 4. In situ FT-IR spectra for (a) $Mo_{(L)}$-$CoMoO_{4-x}$ and (b) $CoMoO_4$. (c) NO_3^-RR reaction path. Bader charge analyses of $CoMoO_4$ (d) and $Mo_{(L)}$-$CoMoO_{4-x}$ (e) surfaces. Comparison of the free energy profiles of NO_3^- to NO_2^- (f) and H_2O dissociation (g) pathways on $CoMoO_4$ and $Mo_{(L)}$-$CoMoO_{4-x}$ surfaces.

contribution to NO_3^--to-NH_3.

DFT calculations were used to in-deep explore the effect of engineering low-valence Mo in $CoMoO_4$ on the performance for NO_3^-RR. The structural model of $CoMoO_4$ and $Mo_{(L)}$-$CoMoO_{4-x}$ were built and showed in Fig. S30. First, the surface electronic structures of $CoMoO_4$ and $Mo_{(L)}$-$CoMoO_{4-x}$ were studied by combining charge-density difference and Bader analysis. As shown in Figs. 4d, 1.32 electrons lost from Co atom to form Co cation site and 2.6 electrons lost from Mo atom to form Mo cation site in $CoMoO_4$. After constructing oxygen vacancies in $CoMoO_4$ ($Mo_{(L)}$-$CoMoO_{4-x}$), the lost electrons number of Co site shows a slight decline to be 1.24, while lost electrons number of Mo site shows a distinct decrease form 2.6–1.5 (Fig. 4e). This difference illustrates that residual electrons derived from oxygen vacancies at pore edge in $Mo_{(L)}$-$CoMoO_{4-x}$ are more prone to localize at Mo site, thus generating the low-valent Mo site, and very few electrons are assigned to Co site. The results are also in agreement with the XPS results of Co 2p (Fig. S8) and Mo 3d (Fig. 1f). Then, the active sites (Co and Mo) on $CoMoO_4$ and $Mo_{(L)}$-$CoMoO_{4-x}$ were identified by analyzing their NO_3^- and H_2O adsorption behaviors. For both $CoMoO_4$ and $Mo_{(L)}$-$CoMoO_{4-x}$, NO_3^- adsorption is spontaneous at Co sites but highly unstable at Mo sites, indicating the adsorption and activation of NO_3^- on both $CoMoO_4$ and $Mo_{(L)}$-$CoMoO_{4-x}$ could occur at Co sites. Furthermore, the NO_3^- adsorption energy on $Mo_{(L)}$-$CoMoO_{4-x}$ (–0.47 eV) is more negative than that on $CoMoO_4$ (–0.16 eV), suggesting the few electrons localization at Co site caused by the oxygen vacancies promote the adsorption of NO_3^- on $Mo_{(L)}$-$CoMoO_{4-x}$ (Fig. S31). In addition, H_2O adsorption sites were also probe. As shown in Fig. S32, the complete coordination of Mo site in $CoMoO_4$ prevents the adsorption of H_2O, thus the H_2O can only absorb at Co site but the adsorption energy is up to 0.6 eV, suggesting the difficult adsorption of H_2O on $CoMoO_4$. In contrast, the H_2O can spontaneously adsorb at low-valent Mo site introduced by oxygen vacancies on $Mo_{(L)}$-$CoMoO_{4-x}$ surface and the adsorption energy is –0.53 eV. This result illustrates that the engineering of low-valent Mo sites provides favorable adsorption site for H_2O, which could generate more *H for NO_3^- hydrogenation.

Typically, NO_3^- electroreduction to NH_3 involves a multielectron/proton transfer process, in which the rate-determining step is the reduction of NO_3^- to NO_2^- [3,59,60]. The Gibbs free energy changes of NO_3^- to NO_2^- pathways on $CoMoO_4$ and $Mo_{(L)}$-$CoMoO_{4-x}$ were further assessed. As shown in Fig. 4f, the spontaneously adsorbed NO_3^- requires energy for further hydrogenation to form *NO_2OH intermediate, and the construction of low-valent Mo lowers the free energy required to form *NO_2OH from 0.25 eV to 0.10 eV, suggesting the thermodynamically favorable activation of NO_3^- on $Mo_{(L)}$-$CoMoO_{4-x}$. Moreover, the free changes of H_2O molecule dissociation on $CoMoO_4$ and $Mo_{(L)}$-$CoMoO_{4-x}$ were calculated and showed in Fig. 4g and S33. The activation energy of H_2O molecule on $Mo_{(L)}$-$CoMoO_{4-x}$ to form the transition state (TS) is 0.66 eV, much lower than that on $CoMoO_4$ (1.0 eV). And the further dissociation of TS to surface-adsorbed *H and *OH species easier on $Mo_{(L)}$-$CoMoO_{4-x}$ is easier. Thus, more active *H could be generated on $Mo_{(L)}$-$CoMoO_{4-x}$, which could have more opportunities to combine with nitrogen-containing intermediates, further promoting ammonia synthesis. All these theoretical results confirm that the construction of low-valent Mo sites in $CoMoO_4$ can promote the adsorption and activation of NO_3^- at the adjacent Co sites, meanwhile, enhance H_2O adsorption and dissociation to generate active *H for the further hydrogenation of NO_3^- to NH_3.

3.4. Electrocatalytic performance for UOR and the coupling reaction

Except for NO_3^-RR, the prepared $Mo_{(L)}$-$CoMoO_{4-x}$ was also exploited as anodic catalyst for urea oxidation reaction (UOR) to more comprehensively treat the wastewater. Typically, 1.0 M KOH solution containing 0.33 M urea was used as the electrolyte. For comparison, the performances of $CoMoO_4$ and NF were also recorded. As demonstrated in Fig. 5a, the $Mo_{(L)}$-$CoMoO_{4-x}$ electrocatalyst shows the most active polarization curve with a high increase in current density and a low potential of 1.31 V vs. RHE at the current density of 100 mA cm^{-2}, which is much lower than those of $CoMoO_4$ (1.43 V vs. RHE) and NF
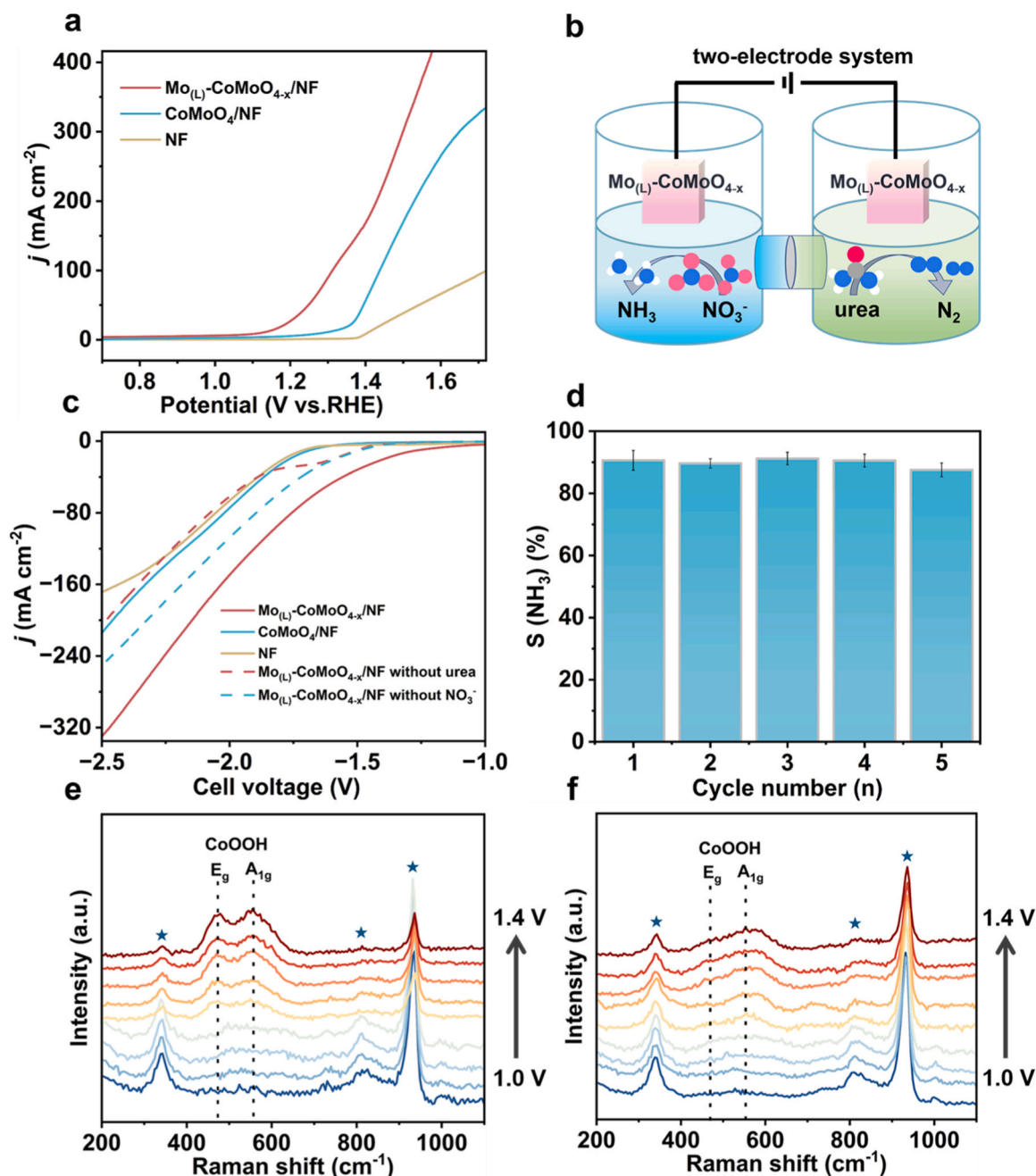
Fig. 5. (a) LSV curves of the prepared samples in 1.0 M KOH with 0.33 M urea electrolyte. (b) Schematic illustration of coupling the anodic UOR with the cathodic NO_3^-RR. (c) The polarization curves of the difunctional materials in 1.0 M KOH with and without NO_3^- and urea. (d) The selectivity of NH_3 for $Mo_{(L)}$-$CoMoO_{4-x}$ at –1.7 V. In situ Raman spectra of $Mo_{(L)}$-$CoMoO_{4-x}$ (e) and $CoMoO_4$ (f) during UOR at different potentials.

(1.72 V vs. RHE), suggesting the good activity of $Mo_{(L)}$-$CoMoO_{4-x}$ for UOR. Furthermore, this excellent UOR performance of $Mo_{(L)}$-$CoMoO_{4-x}$ is also superior to most reported UOR electrocatalysts (Table S2). Profiting from the excellent UOR performance, we coupled the anodic UOR with the cathodic NO_3^-RR to assemble the two-electrode electrolyzer to improve the energy efficiency of N-containing wastewater treatment (Fig. 5b). The polarization curves of the different electrocatalysts in 1.0 M KOH with and without NO_3^- and urea were recorded in Fig. 5c. The $Mo_{(L)}$-$CoMoO_{4-x}$ exhibited the largest current density at the present of both NO_3^- and urea and the current density could reach to 100 mA cm^{-2} under a low potential of –1.83 V. And the selectivity of NH_3 could retain over 90% at wide potential from –1.4 to –1.9 V (Fig. S34). Additionally, no apparent decrease of the selectivity of NH_3 is observed after five cycle runs at –1.7 V, indicating the excellent

durability (Fig. 5d). The low cell voltage and good stability of $Mo_{(L)}$-$CoMoO_{4-x}$ for the coupling electrolysis suggested its great potential for practical application of N-containing wastewater treatment. To further unravel the good activity of $Mo_{(L)}$-$CoMoO_{4-x}$ for UOR, in situ Raman test was carried out. As shown in Fig. 5e, three typical bands at 341, 809, 933 cm^{-1} were assigned to the O-Mo-O and Co-O-Mo in $Mo_{(L)}$-$CoMoO_{4-x}$, respectively. And their intensities decreased gradually with increasing potential from 1.0 to 1.4 V vs. RHE. Meanwhile, two characteristic peaks located at 473 and 553 cm^{-2}, which could be assigned to the E_g and A_{1g} of CoOOH respectively [61,62], were detected and the intensities increased gradually with increasing potential, suggesting the evolution of $Mo_{(L)}$-$CoMoO_{4-x}$ to the active CoOOH during UOR. This reconstruction phenomenon could also be observed in the Raman spectra of $CoMoO_4$ (Fig. 5f), but the intensity of the restructured CoOOH

signal was much weaker than that of $Mo_{(L)}$-$CoMoO_{4-x}$. The compared Raman results revealed that the excellent UOR activity of $Mo_{(L)}$-$CoMoO_{4-x}$ could be attributed to the construction of low-valent Mo in $CoMoO_4$ could efficiently promote the generation of active CoOOH for UOR.

4. Conclusion

In summary, we have exploited a difunctional electrocatalyst of porous $CoMoO_4$ nanosheets with rich low-valent Mo sites grown on Ni foam for both NO_3^- and urea-contained wastewater treatment. The low-valent Mo sites induced by the rich pores and oxygen vacancies in $CoMoO_4$ nanosheets promote the adsorption and activation of NO_3^- at the adjacent Co sites for the accelerated reaction NO_3RR, meanwhile, enhance H_2O adsorption and dissociation to generate active *H for the generation of the key NH_2OH intermediate of NO_3^- to NH_3. As expected, the $Mo_{(L)}$-$CoMoO_{4-x}$ showed superior performance toward NO_3RR with a high Faradaic efficiency (93.33%)and selectivity (91.16%) at –1.1 V vs. Ag/AgCl in 0.1 M Na_2SO_4 with 200 ppm NO_3^--N, much better than those of $CoMoO_4$. In addition, more active CoOOH could be restructured in $Mo_{(L)}$-$CoMoO_{4-x}$ render it also exhibited excellent UOR activity with an ultralow potential (1.31 V vs. RHE) at 100 mA cm^{-2}, surpassing the $CoMoO_4$ and most reported electrocatalysts. Additionally, the bifunctional $Mo_{(L)}$-$CoMoO_{4-x}$ electrodes can be assembled into a two-electrode electrolyzer for coupling the UOR with NO_3RR, and a low cell voltage of –1.83 V was needed to reach the current density of 100 mA cm^{-2}, and the selectivity of NH_3 can remain over 90% after five cycles. This work provides a novel and economic strategy for nitrogen-rich wastewater treatment and opens an avenue to design efficient difunctional electrocatalysts for electrochemical UOR and NO_3^--to-NH_3.

CRediT authorship contribution statement

Shan Gao: Funding acquisition. **Qiquan Luo:** Investigation. **Weitao He:** Data curation. **Xing Chen:** Investigation. **Yu Cheng:** Investigation. **Kaifu Zhang:** Data curation. **Yu Yu:** Writing – review & editing, Writing – original draft, Data curation, Conceptualization. **Yuan Li:** Funding acquisition, Data curation.

Declaration of Competing Interest

The authors declare that they have no known competing financial interests or personal relationships that could have appeared to influence the work reported in this paper.

Data Availability

No data was used for the research described in the article.

Acknowledgements

Appendix A. Supporting information

Supplementary data associated with this article can be found in the online version at doi:10.1016/j.apcatb.2024.124150.

References

[1] H. Xu, Y.Y. Ma, J. Chen, W.X. Zhang, J.P. Yang, Electrocatalytic reduction of nitrate-a step towards a sustainable nitrogen cycle, Chem. Soc. Rev. 51 (2022) 2710–2758.

[2] P.H. Van Langevelde, I. Katsounaros, M.T.M. Koper, Electrocatalytic nitrate reduction for sustainable ammonia production, Joule 5 (2021) 290–294.

[3] S.H. Han, H.J. Li, T.L. Li, F.P. Chen, R. Yang, Y.F. Yu, B. Zhang, Ultralow overpotential nitrate reduction to ammonia via a three-step relay mechanism, Nat. Catal. 6 (2023) 402–414.

[4] Y.P. Zhai, B.W. Zhang, S.Y. Zhang, Y. Liu, B.Y. Wang, K. Zhang, G.I.N. Waterhouse, T.R. Zhang, S.Y. Lu, Carbon dots as new building blocks for electrochemical energy storage and electrocatalysis, Adv. Energy Mater. 12 (2022) 2103426.

[5] H.Q. Song, J.K. Yu, Z.Y. Tang, B. Yang, S.Y. Lu, Halogen-doped carbon dots on amorphous cobalt phosphide as robust electrocatalysts for overall water splitting, Adv. Energy Mater. 12 (2022) 2102573.

[6] H.Q. Song, M. Wu, Z.Y. Tang, J.S. Tse, B. Yang, S.Y. Lu, Single atom ruthenium-doped CoP/CDs nanosheets via splicing of carbon-dots for robust hydrogen production, Angew. Chem. Int. Ed. 60 (2021) 7234–7244.

[7] Z.M. Song, Y. Liu, Y.Z. Zhong, Q. Guo, J. Zeng, Z.G. Geng, Efficient electroreduction of nitrate into ammonia at ultralow concentrations via an enrichment effect, Adv. Mater. 34 (2022) 2204306.

[8] Y.F. Ren, F.G. Tian, L.M. Jin, Y. Wang, J.P. Yang, S.J. You, Y.B. Liu, Fluidic MXene electrode functionalized with iron single atoms for selective electrocatalytic nitrate transformation to ammonia, Environ. Sci. Technol. 57 (2023) 10458–10466.

[9] R. Zhang, C. Li, H.L. Cui, Y.B. Wang, S.C. Zhang, P. Li, Y. Hou, Y. Guo, G.J. Liang, Z. D. Huang, C. Peng, C.Y. Zhi, Electrochemical nitrate reduction in acid enables high-efficiency ammonia synthesis and high-voltage pollutes-based fuel cells, Nat. Commun. 14 (2023) 8036.

[10] A. Zhang, Y.X. Liang, H. Zhang, Z.G. Geng, J. Zeng, Doping regulation in transition metal compounds for electrocatalysis, Chem. Soc. Rev. 50 (2021) 9817–9844.

[11] E. Murphy, Y.C. Liu, I. Matanovic, M. Rüscher, Y. Huang, A. Ly, S. Guo, W.J. Zang, X.X. Yan, A. Martini, Elucidating electrochemical nitrate and nitrite reduction over atomically-dispersed transition metal sites, Nat. Commun. 14 (2023) 4554.

[12] X. Zheng, J. Yang, P. Li, Z. Jiang, P. Zhu, Q. Wang, J. Wu, E. Zhang, W. Sun, S. Dou, D. Wang, Y. Li, Dual-atom support boosts nickel-catalyzed urea electrooxidation, Angew. Chem. Int. Ed. 62 (2023) e202217449.

[13] X.T. Gao, S. Zhang, P.T. Wang, M. Jaroniec, Y. Zheng, S.Z. Qiao, Urea catalytic oxidation for energy and environmental applications, Chem. Soc. Rev. 53 (2024) 1552–1591.

[14] L. Fang, S. Wang, S. Lu, F.J. Yin, Y.J. Dai, L. Chang, H. Liu, Efficient electroreduction of nitrate via enriched active phases on copper-cobalt oxides, Chem. Eng. J. 461 (2023) 108864.

[15] S. Gao, Y. Lin, X.C. Jiao, Y.F. Sun, Q.Q. Luo, W.H. Zhang, D.Q. Li, J.L. Yang, Y. Xie, Partially oxidized atomic cobalt layers for carbon dioxide electroreduction to liquid fuel, Nature 529 (2016) 68–71.

[16] Y.F. Ren, S.J. You, Y. Wang, J.P. Yang, Y.B. Liu, Bioinspired tandem electrode for selective electrocatalytic synthesis of ammonia from aqueous nitrate, Environ. Sci. Technol. 58 (2024) 2144–2152.

[17] G.K. Zhang, X.T. Li, K. Chen, Y.L. Guo, D.W. Ma, K. Chu, Tandem electrocatalytic nitrate reduction to ammonia on MBenes, Angew. Chem. Int. Ed. 62 (2023) e202300054.

[18] K. Fan, W.F. Xie, J.Z. Li, Y.N. Sun, P.C. Xu, Y. Tang, Z.H. Li, M.F. Shao, Active hydrogen boosts electrochemical nitrate reduction to ammonia, Nat. Commun. 13 (2022) 7958.

[19] Y. Zhou, Y.M. Wang, D.Q. Kong, Q.Q. Zhao, L. Zhao, J.L. Zhang, X.M. Chen, Y.A. Li, Y. Xu, C. Meng, Revealing the reactant mediation role of low-valence Mo for accelerated urea-assisted water splitting, Adv. Funct. Mater. 33 (2023) 2210656.

[20] H.J. Liu, S. Zhang, Y.M. Chai, B. Dong, Ligand modulation of active sites to promote cobalt-doped 1T-MoS_2 electrocatalytic hydrogen evolution in alkaline media, Angew. Chem. Int. Ed. 62 (2023) e202313845.

[21] Y.K. Bai, F. Wu, X.C. Zhou, Y.F. Ye, K.Q. Nie, Jo Wang, M. Xie, Z.X. Zhang, Z.J. Liu, T. Cheng, Promoting nickel oxidation state transitions in single-layer NiFeB hydroxide nanosheets for efficient oxygen evolution, Nat. Commun. 13 (2022) 6094.

[22] F.Y. Chen, Z.Y. Wu, S. Gupta, D.J. Rivera, S.V. Lambeets, S. Pecaut, J.Y.T. Kim, P. Zhu, Y.Z. Finfrock, D.M. Meira, Efficient conversion of low-concentration nitrate sources into ammonia on a Ru-dispersed Cu nanowire electrocatalyst, Nat. Nanotechnol. 17 (2022) 759–767.

[23] Y.T. Wang, Y.F. Yu, R.R. Jia, C. Zhang, B. Zhang, Electrochemical synthesis of nitric acid from air and ammonia through waste utilization, Natl. Sci. Rev. 6 (2019) 730–738.

[24] G. Kresse, J. Furthmüller, Efficiency of Ab-initio total energy calculations for metals and semiconductors using a plane-wave basis set, Comput. Mater. Sci. 6 (1996) 15–50.

[25] G. Kresse, J. Furthmüller, Efficient iterative schemes for Ab initio total-energy calculations using a plane-wave basis set, Phys. Rev. B 54 (1996) 11169–11186.

[26] P.E. Blöchl, Projector augmented-wave method, Phys. Rev. B 50 (1994) 17953–17979.

[27] B. Hammer, L.B. Hansen, J.K. Nørskov, Improved adsorption energetics within density-functional theory using revised perdew-burke-ernzerhof functionals, Phys. Rev. B 59 (1999) 7413–7421.

[28] M.Q. He, X. Chen, Y.N. Zhou, C. Xu, X.X. Li, Q.Q. Luo, J.L. Yang, A first-principles study of regulating spin states of $MoSi_2N_4$ supported single-atom catalysts via doping strategy for enhancing electrochemical nitrogen fixation activity, J. Phys. Chem. Lett. 14 (2023) 7100–7107.

[29] S.P. Geng, L.M. Chen, H.X. Chen, Y. Wang, Z.B. Ding, D.D. Cai, S.Q. Song, Revealing the electrocatalytic mechanism of layered crystalline CoMoO4 for water splitting: a theoretical study from facet selecting to active site engineering, Chin. J. Catal. 50 (2023) 334–342.

[30] G. Henkelman, B.P. Uberuaga, H. Jónsson, A climbing image nudged elastic band method for finding saddle points and minimum energy paths, J. Chem. Phys. 113 (2000) 9901–9904.

[31] J.A. Gauthier, C.F. Dickens, L.D. Chen, A.D. Doyle, J.K. Nørskov, Solvation effects for oxygen evolution reaction catalysis on IrO2(110), J. Phys. Chem. C. 121 (2017) 11455–11463.

[32] X.Y. Zhu, M.Q. He, X. Chen, Y.A. Zhou, C. Xu, X.X. Li, Q.Q. Luo, J.L. Yang, First-principles insights into tungsten semicarbide-based single-atom catalysts: single-atom migration and mechanisms in oxygen reduction, J. Phys. Chem. Lett. 15 (2024) 2815–2824.

[33] S.J. Guo, K. Heck, S. Kasiraju, H.F. Qian, Z. Zhao, L.C. Grabow, J.T. Miller, M. S. Wong, Insights into nitrate reduction over indium-decorated palladium nanoparticle catalysts, ACS Catal. 8 (2018) 503–515.

[34] R.R. Zhang, L. Pan, B.B. Guo, Z.F. Huang, Z.X. Chen, L. Wang, X.W. Zhang, Z. Y. Guo, W. Xu, K.P. Loh, Tracking the role of defect types in Co3O4 structural evolution and active motifs during oxygen evolution reaction, J. Am. Chem. Soc. 145 (2023) 2271–2281.

[35] H.B. Xiao, K. Chi, H.X. Yin, X.J. Zhou, P.X. Lei, P.Z. Liu, J.K. Fang, X.H. Li, S. L. Yuan, Z. Zhang, Excess activity tuned by distorted tetrahedron in CoMoO4 for oxygen evolution, Energy Environ. Sci. (2023) e12495.

[36] Z. Tang, Y.J. Li, K.X. Zhang, X.X. Wang, S.Y. Wang, Y.F. Sun, H.Y. Zhang, S.Y. Li, J. R. Wang, X.Y. Gao, Interfacial hydrogen spillover on Pd-TiO2 with oxygen vacancies promotes formate electrooxidation, ACS Energy Lett. 8 (2023) 3945–3954.

[37] Y. Wang, R. Yang, Y.J. Ding, B. Zhang, H. Li, B. Bai, M.R. Li, Y. Cui, J.P. Xiao, Z. S. Wu, Unraveling oxygen vacancy site mechanism of Rh-doped RuO2 catalyst for long-lasting acidic water oxidation, Nat. Commun. 14 (2023) 1412.

[38] Y. Qi, B.W. Liu, X.Q. Qiu, X.Z. Zeng, Z.C. Luo, W.D. Wu, Y.C. Liu, L.H. Chen, X. H. Zu, H.F. Dong, Simultaneous oxidative cleavage of lignin and reduction of furfural via efficient electrocatalysis by P-doped CoMoO4, Adv. Mater. 35 (2023) 2208284.

[39] D.Y. Li, R. Xiang, F. Yu, J.S. Zeng, Y. Zhang, W.C. Zhou, L.L. Liao, Y. Zhang, D. S. Tang, H.Q. Zhou, Situ regulating cobalt/iron oxide-oxyhydroxide exchange by dynamic iron incorporation for robust oxygen evolution at large current density, Adv. Mater. (2023) 2305685.

[40] Y.T. Wang, H.J. Li, W. Zhou, X. Zhang, B. Zhang, Y.F. Yu, Structurally disordered RuO2 nanosheets with rich oxygen vacancies for enhanced nitrate electroreduction to ammonia, Angew. Chem. Int. Ed. 134 (2022) e202202604.

[41] J.Y. Fang, Q.Z. Zheng, Y.Y. Lou, K.M. Zhao, S.N. Hu, G. Li, O. Akdim, X.Y. Huang, S.G. Sun, Ampere-level current density ammonia electrochemical synthesis using CuCo nanosheets simulating nitrite reductase bifunctional nature, Nat. Commun. 13 (2022) 7899.

[42] L.R. Mi, Q.H. Huo, J.Y. Cao, X.B. Chen, H.P. Yang, Q. Hu, C.X. He, Achieving synchronization of electrochemical production of ammonia from nitrate and ammonia capture by constructing a "two-in-one" flow cell electrolyzer, Adv. Energy Mater. 12 (2022) 2202247.

[43] R. Mao, C. Huang, X. Zhao, M. Ma, J.H. Qu, Dechlorination of triclosan by enhanced atomic hydrogen-mediated electrochemical reduction: kinetics, mechanism, and toxicity assessment, Appl. Catal. B Environ. 241 (2019) 120–129.

[44] W.H. He, J. Zhang, S. Dieckhöfer, S. Varhade, A.C. Brix, A. Lielpetere, S. Seisel, J.R. C. Junqueira, W. Schuhmann, Splicing the active phases of copper/cobalt-based catalysts achieves high-rate tandem electroreduction of nitrate to ammonia, Nat. Commun. 13 (2022) 1129.

[45] Q.N. Song, M. Li, X.S. Hou, J.C. Li, Z.J. Dong, S. Zhang, L. Yang, X. Liu, Anchored Fe atoms for NO bond activation to boost electrocatalytic nitrate reduction at low concentrations, Appl. Catal. B Environ. 317 (2022) 121721.

[46] M. Liu, Z.H. Lu, L.H. Yang, R.M. Gao, X.Y. Zhang, Y.J. Wang, Y.H. Wang, Co-N bond promotes the H* pathway for the electrocatalytic reduction of nitrate (NO3RR) to ammonia, J. Environ. Chem. Eng. 11 (2023) 109718.

[47] R. Chauhan, V.C. Srivastava, Electrochemical denitrification of highly contaminated actual nitrate wastewater by Ti/RuO2 anode and iron cathode, Chem. Eng. J. 386 (2020) 122065.

[48] J. Li, G.M. Zhan, J.H. Yang, F.J. Quan, C.L. Mao, Y. Liu, B. Wang, F.C. Lei, L.J. Li, A. W. Chan, Efficient ammonia electrosynthesis from nitrate on strained ruthenium nanoclusters, J. Am. Chem. Soc. 142 (2020) 7036–7046.

[49] R.X. Ge, Y. Wang, Z.Z. Li, M. Xu, S.M. Xu, H. Zhou, K.Y. Ji, F.G. Chen, J.H. Zhou, H. H. Duan, Selective electrooxidation of biomass-derived alcohols to aldehydes in a neutral medium: promoted water dissociation over a nickel-oxide-supported ruthenium single-atom catalyst, Angew. Chem. Int. Ed. 134 (2022) e202200211.

[50] H. Guo, M.Y. Li, Y.T. Yang, R. Luo, W. Liu, F.Y. Zhang, C. Tang, G.D. Yang, Y. Zhou, Self-supported Pd nanorod arrays for high-efficient nitrate electroreduction to ammonia, Small 19 (2023) 2207743.

[51] G.K. Zhang, F.Z. Wang, K. Chen, Jl Kang, K. Chu, Atomically dispersed Sn confined in FeS2 for nitrate-to-ammonia electroreduction, Adv. Funct. Mater. 34 (2023) 2305372.

[52] Y.L. Wang, H.B. Yin, F. Dong, X.G. Zhao, Y.K. Qu, L.X. Wang, Y. Peng, D.S. Wang, W. Fang, J.H. Li, N-coordinated Cu–Ni dual-single-atom catalyst for highly selective electrocatalytic reduction of nitrate to ammonia, Small 19 (2023) 2207695.

[53] J. Zhou, S.H. Han, R. Yang, T.L. Li, W.B. Li, Y.T. Wang, Y.F. Yu, B. Zhang, Linear adsorption enables NO selective electroreduction to hydroxylamine on single Co sites, Angew. Chem. Int. Ed. 62 (2023) e202305184.

[54] W.S. Gao, K.F. Xie, J. Xie, X.M. Wang, H. Zhang, S.Q. Chen, H. Wang, Z.L. Li, C. Li, Alloying of Cu with Ru Enabling the Relay Catalysis for Reduction of Nitrate to Ammonia, Adv. Mater. 35 (2023) 2202952.

[55] R.D. Zhao, Q.Y. Yan, L.H. Yu, T. Yan, X.Y. Zhu, Z.Y. Zhao, L. Liu, J.Y. Xi, A Bi-Co corridor construction effectively improving the selectivity of electrocatalytic nitrate reduction towards ammonia by nearly 100%, Adv. Mater. 35 (2023) 2306633.

[56] X.F. Cheng, J.H. He, H.Q. Ji, H.Y. Zhang, Q. Cao, W.J. Sun, C.L. Yan, J.M. Lu, Coordination symmetry breaking of single-atom catalysts for robust and efficient nitrate electroreduction to ammonia, Adv. Mater. 34 (2022) 2205767.

[57] Y.T. Wang, C.H. Wang, M.Y. Li, Y.F. Yu, B. Zhang, Nitrate electroreduction: mechanism insight, in situ characterization, performance evaluation, and challenges, Chem. Soc. Rev. 50 (2021) 6720–6733.

[58] Y.T. Wang, W. Zhou, R.R. Jia, Y.F. Yu, B. Zhang, Unveiling the activity origin of a copper-based electrocatalyst for selective nitrate reduction to ammonia, Angew. Chem. Int. Ed. 59 (2020) 5350–5354.

[59] Y.G. Bu, C. Wang, W.K. Zhang, X.H. Yang, J. Ding, G.D. Gao, Electrical pulse-driven periodic self-repair of Cu-Ni tandem catalyst for efficient ammonia synthesis from nitrate, Angew. Chem. Int. Ed. 62 (2023) e202217337.

[60] E. Murphy, Y.C. Liu, I. Matanovic, M. Rüscher, Y. Huang, A. Ly, S.Y. Guo, W. J. Zang, X.X. Yan, A. Martini, J. Timoshenko, B.R. Cuenya, I.V. Zenyuk, X.Q. Pan, E.D. Spoerke, P. Atanassov, Elucidating electrochemical nitrate and nitrite reduction over atomically-dispersed transition metal sites, Nat. Commun. 14 (2023) 4554.

[61] H.X. Yin, H.B. Xiao, R.M. Qin, J. Chen, F. Tan, W. Zhang, J. Zhao, L. Zeng, Y.F. Hu, F. Pan, P.X. Lei, S.L. Yuan, L.H. Qian, Y.Q. Su, Z. Zhang, Lattice strain mediated reversible reconstruction in CoMoO4·0.69H2O for intermittent oxygen evolution, ACS Appl. Mater. Interfaces 15 (2023) 20100–20109.

[62] H.B. Xiao, K. Chi, H.X. Yin, X.J. Zhou, P.X. Lei, P.Z. Liu, J.K. Fang, X.H. Li, S. L. Yuan, Z. Zhang, Y.Q. Su, J.J. Guo, L.H. Qian, Excess activity tuned by distorted tetrahedron in CoMoO4 for oxygen evolution, Energy Environ. Mater. (2023) e12495.